

Local Influences of Transient Basicity Segregation in Iron-Bearing Materials on Softening and Melting in Blast Furnaces at High Temperatures



ZHEHAN LIAO, KAI WANG, YIZHANG YANG, ZHAOJIE TENG, PANSHUAI MA, QINGHUI WU, SHENGLI WU, and JIAN XU

The distribution of iron-bearing granular materials in the throat of a blast furnace (BF) plays a crucial role in influencing their performance at high temperatures. Therefore, it is essential to establish a quantitative relationship between the charging operation of the iron-bearing materials at ambient temperatures and their subsequent softening and melting behaviors at elevated temperatures. In this study, the discrete element method (DEM) is employed to quantify the instantaneous mass segregation of quaternary iron-bearing materials throughout the continuous charging process, starting from the feeding conveyor belt and continuing up to the throat. Subsequently, employing quaternary basicity (R_4) as a pivotal bridge, softening and melting experiments (the temperature above 900 °C and in an atmosphere with a mole fraction of 30 pct CO to 70 pct N₂) are conducted to assess the influence of physical segregation on chemical performances under simulated BF conditions. The results reveal that the sequence of loading quaternary iron-bearing materials onto the feeding belt causes fluctuations in R_4 , ranging from 1.08 to 1.75. Moreover, these fluctuations are propagated throughout the charging process, resulting in notable fluctuations in the mass fractions of iron-bearing materials and the R_4 at the hopper outlet and the end of the chute. Therefore, the primary factor influencing the flowing characteristics of the granular materials is their distribution within the hopper. Then, the segregation in the throat is further characterized by the presence of two distinct R_4 ranges (1.2 to 1.29, and 1.3 to 1.39) observed across a total of 48 equal-area blocks, and the significant difference between these two categories is determined by sinters. Besides, the influence of the R_4 on softening and melting temperatures is quantitatively evaluated, resulting in a 'w'-shaped temperature distribution from the center to the edge of the BF. Our findings provide evidence of the inadequacy of evaluating the softening and melting behaviors of iron-bearing materials solely based on their initial proportions in the structure of iron-bearing materials. Instead, a quantitative examination of the granular segregation in the throat, arising from the BF charging operation, is deemed essential to provide substantial support for well-designed elevated-temperature experiments. This approach enables a more comprehensive understanding of the intricate journey of iron-bearing materials in the BF.

<https://doi.org/10.1007/s11663-024-03121-2>

© The Minerals, Metals & Materials Society and ASM International 2024

I. INTRODUCTION

THE blast furnace (BF) operates as a multi-phase counter-flow reactor, efficiently reducing iron-bearing materials to produce hot metal.^[1–4] The distribution of granular materials within the BF is significantly influenced by the charging operation, thereby affecting gas flow, heat transfer, and reaction efficiency. As a result, extensive efforts have been devoted to achieving a comprehensive understanding of granular segregation behaviors during the charging process *via* industrial-scale measurements,^[5] lab-scale experiments,^[6–8] mathematical model analysis,^[9–11] and discrete element method (DEM) simulations.^[12–14]

ZHEHAN LIAO, YIZHANG YANG, PANSHUAI MA, QINGHUI WU, and JIAN XU are with the College of Materials Science and Engineering, Chongqing University, Chongqing 400044, P.R. China. Contact e-mail: jxu@cqu.edu.cn KAI WANG is with the School of Metallurgical and Ecological Engineering, University of Science and Technology Beijing, Beijing 100083, P.R. China and also with the Beijing Shougang Co., Ltd., Qianan 064404, P.R. China. ZHAOJIE TENG is with the Shougang Jingtang United Iron and Steel Co., Ltd., Tangshan 063200, P.R. China. SHENGLI WU is with the School of Metallurgical and Ecological Engineering, University of Science and Technology Beijing and also with the Shougang Jingtang United Iron and Steel Co., Ltd.

Manuscript submitted October 25, 2023; accepted April 22, 2024.
Article published online May 15, 2024.

The continuous charging process of the BF can be divided into three key stages. In the first stage, iron-bearing granular materials are loaded onto a conveyor belt, where the specific charging sequence induces the onset of granular segregation.^[15] In addition, the placement of the main feeding belt influences the trajectory of granular motion within the hopper.^[16] Moving to the second stage, the iron-bearing granular materials are charged into a hopper where the hopper's shape and size directly impact the flow dynamics of the granular materials. For a wedge-shaped hopper, smaller granules demonstrate enhanced efficiency in converting kinetic energy during discharge.^[17] Simultaneously, the slope of the lower part of the hoppers affects granular size distribution exclusively during the discharge process.^[18] Furthermore, when granular materials are charged into a conical-shaped hopper, mass discharge rates reduce granular segregation during hopper discharge.^[19,20] Subsequently, the granules will pass through a Y-shaped tube. However, the motion and segregation behaviors of the granules are not influenced by the angle of the Y-shaped tube.^[21] Entering the third stage, the iron-bearing granular materials reach the BF throat through a rotating chute. The trajectory of the flowing granular materials is primarily influenced by centrifugal and Coriolis forces exerted on the granules by the rotating chute.^[12,22] The interaction between chute curvature and the Coriolis force led to circumferential mass, size, and porosity segregation^[23–30] which is also affected by the effective lengths of chutes,^[24] the size ratio,^[31] and so on. In addition, the chute shape also played a critical role, with a rectangular-shaped chute promoting a uniform circumferential distribution of granular materials, whereas a trapezoidal chute encouraged aggregation at lower rotating speeds.^[25,32]

After the iron-bearing materials are discharged, these materials descend further, and as the temperature in the furnace increases, these materials begin to soften and melt, and form a cohesive zone.^[33,34] The cohesive zone, however, exhibits poor permeability, which directly affects the gas flow re-distributed within the furnace.^[35] Therefore, softening and melting tests^[36–40] are widely used to provide assessments of how iron-bearing materials perform in the high temperature of a BF. For single-component materials, an increase in the basicity of sinters leads to a deterioration in both pressure drop and permeability.^[41,42] Conversely, increasing the MgO content of pellets enhances their high-temperature properties.^[43] Moreover, it is widely acknowledged that lump ores perform inferior to sinters at high temperatures.^[44] In addition, the softening and melting temperatures of the samples increased with increasing basicity under different atmospheres.^[45] However, high-temperature interaction between iron-bearing materials can improve the softening and melting characteristics.^[46] Specifically, the interaction behaviors between lump ores and sinters^[44] can significantly improve the softening temperature of lump ores, and the softening and melting properties of the oxidized pellets are

dramatically improved by the interaction between oxidized pellets and metalized pellets.^[47] However, there is no obvious interaction between lump ore and pellets, pellets and pellets, and lump ore and lump ore.^[48]

Undoubtedly, the granular segregation of iron-bearing materials in the BF throat has a vital impact on their chemical reactions at high temperatures. Although previous studies have provided comprehensive insights into granular segregation behaviors, a critical gap remains in establishing a comprehensive connection between the physical segregations resulting from the charging operation and the subsequent chemical performances in the BF. To address this gap, this study first employs the DEM to simulate the granular flow behaviors of quaternary iron-bearing materials, including sinters, alkaline pellets, acid pellets, and lump ores, during the continuous charging process. The quaternary basicity (extended Vee ratio^[49]), denoted as $R_4 = \frac{\text{wt}(\text{CaO}) + \text{wt}(\text{MgO})}{\text{wt}(\text{SiO}_2) + \text{wt}(\text{Al}_2\text{O}_3)}$, where $\text{wt}(\text{CaO})$, $\text{wt}(\text{MgO})$, $\text{wt}(\text{SiO}_2)$, and $\text{wt}(\text{Al}_2\text{O}_3)$ represent the mass fractions of CaO, MgO, SiO₂, and Al₂O₃, respectively, serves as a key link enabling the elaborate design of schemes for subsequent softening and melting experiments to evaluate the performance of iron-bearing materials with different proportions at temperatures above 900 °C and in an atmosphere with a mole fraction of 30 pct CO to 70 pct N₂. This study pioneers an innovative approach to bridge the gap between iron-bearing materials' charging operation and iron-bearing materials' softening and melting behaviors, shedding light on how the physical behaviors of granular materials during the charging process profoundly influence their chemical performance at elevated temperatures.

II. EXPERIMENTAL PROCEDURE

A. Iron-Bearing Granular Materials

The quaternary iron-bearing granular materials include sinters, alkaline pellets, acid pellets, and lump ores. Their physical properties and chemical compositions are summarized in Tables I and II, respectively.

B. Softening and Melting Experiments

In Figure 1(a), a schematic diagram of the apparatus utilized for the softening and melting experiments is presented. To conduct the experiments, 150 g of iron-bearing granular materials are sandwiched between two layers of 15 g of cokes within a graphite crucible, as depicted in Figure 1(b). The graphite crucible features nine uniformly distributed holes with a diameter of 6 mm at its bottom. Subsequently, the crucible is placed in the furnace and heated from the ambient temperature to 1500 °C as the heating rate is explained in Figure 1(c). Notably, a reducing gas mixture (30 pct CO to 70 pct N₂ in mole fraction) instead of an inert gas (100 pct N₂), is

Table I. Physical Properties of Quaternary Iron-Bearing Granular Materials





Properties	Sinters	Alkaline Pellets	Acid Pellets	Lump Ores
Density, ρ (kg/m ³)	3300	3948	3948	2850
Weight Per Batch, m (kg/batch)	70732	52751	42856	10669
Average Diameter, d (m)	0.025	0.016	0.016	0.025
Appearance				

Table II. Chemical Compositions of Quaternary Iron-Bearing Granular Materials (Wt Pct)

	TFe	SiO ₂	CaO	MgO	Al ₂ O ₃	S	TiO ₂	FeO	K ₂ O	ZnO	Na ₂ O	P	R ₄
Sinters	55.84	5.51	10.68	2.08	1.77	0.02	0.12	8.7	0.05	0.02	0.06	0.07	1.74
Alkaline pellets	65.94	2.28	2.49	0.63	0.53	0.04	0.07	0.55	0.04	0.01	0.09	0.01	1.11
Acid Pellets	66.33	2.87	0.60	0.68	0.66	0.01	0.08	0.42	0.09	0.01	0.10	0.01	0.36
Lump Ores	62.58	3.18	0.11	0.03	1.54	0.02	0.07	—	—	—	—	—	0.03

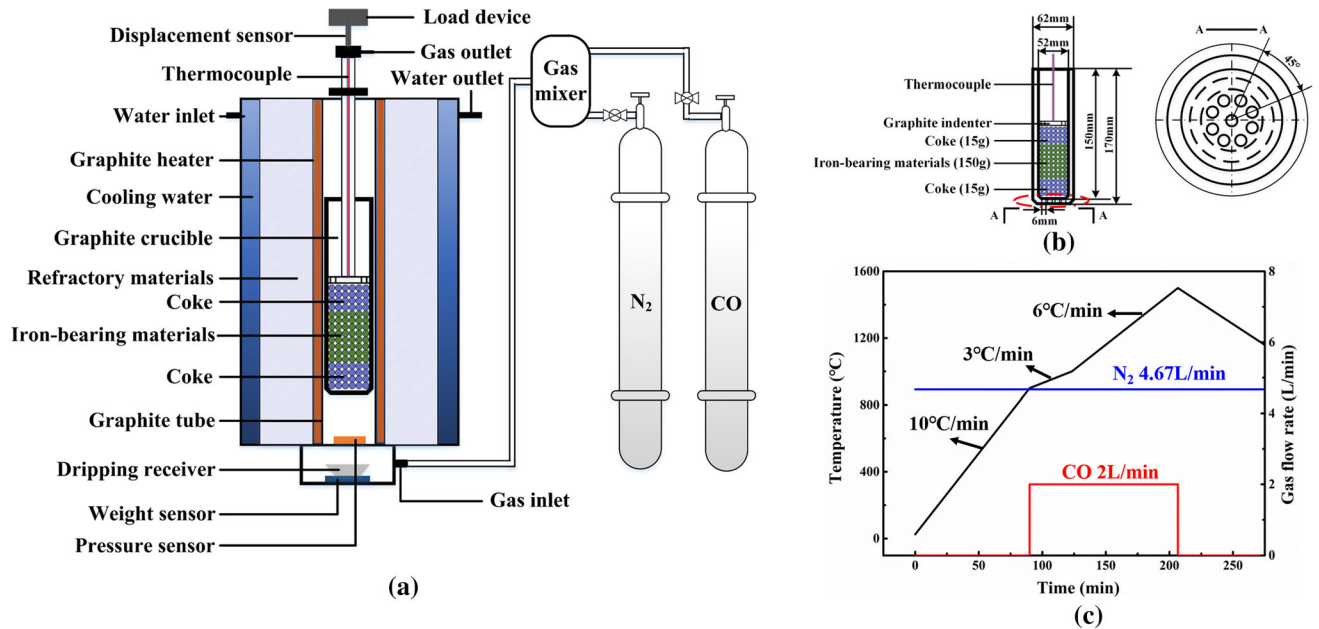


Fig. 1—(a) A schematic diagram of the apparatus for the softening and melting experiments, (b) the sandwiched packed bed in a graphite crucible, and (c) the specific experimental conditions.

injected into the furnace once the samples have reached 900 °C. In addition, a displacement sensor records the instantaneous shrinkage of the sandwich-like packed bed, a pressure sensor captures the instantaneous pressure drop, and a weight sensor records the weight of drippings. Further details on the softening and melting experiments can be found in previous studies.^[50–53]

III. NUMERICAL SIMULATION CONDITIONS

A 5500 m³ full-scale bell-less top model of BF with two parallel hoppers is established in Figure 2(a). It consists of six main parts arranged from top to bottom: the feeding system, receiving hopper, two parallel hoppers, central throat tube, rotating chute, and throat. In particular, Figure 2(b) provides a further explanation of the feeding system. The granular materials are initially charged onto the B-2 belt (80.52 m in length and 2.20 m in width). Before being discharged into the

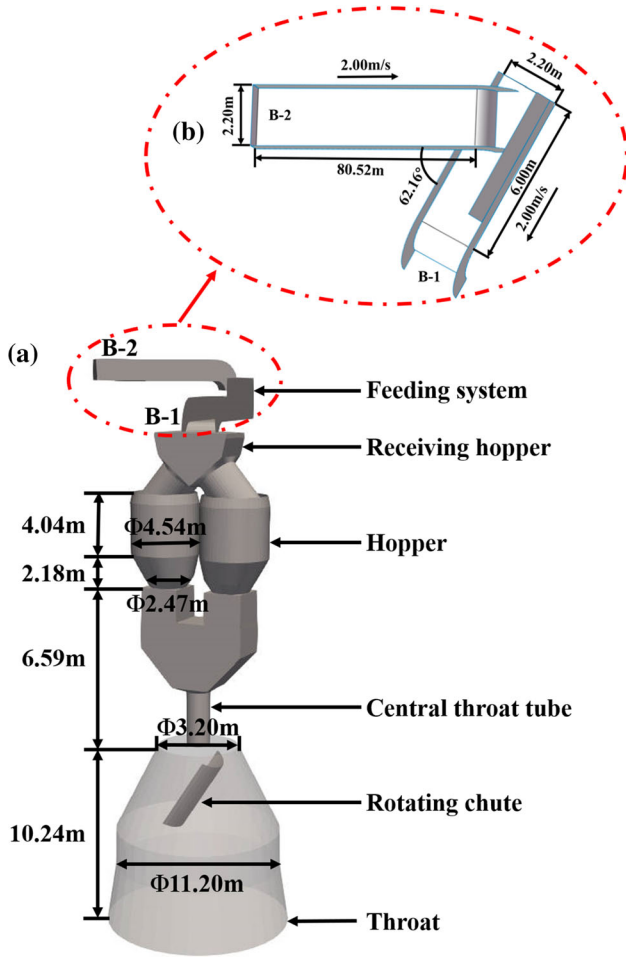


Fig. 2—(a) A full-scale bell-less top model of BF with two parallel hoppers and (b) a detailed explanation of the feeding system.

receiving hopper, they are subsequently conveyed onto the B-1 belt (6.00 m in length) at the end of the B-2 belt. The minimum angle between the two crossed belts is 62.16 deg, and both belts maintain a velocity of 2.00 m/s.

In addition, the charging process of quaternary iron-bearing granular materials is simulated by the DEM.^[54] Briefly, the Newton's equations of motion are used to determine the translational and rotational motions of each particle:

$$m_i \frac{d\mathbf{u}_i}{dt} = \sum_{j=1}^K (\mathbf{F}_{n,ij} + \mathbf{F}_{t,ij}) + m_i \mathbf{g}, \quad [1]$$

$$I_i \frac{d\boldsymbol{\omega}_i}{dt} = \sum_{j=1}^K (\mathbf{T}_{t,ij} + \mathbf{T}_{r,ij}), \quad [2]$$

where m_i , I_i , \mathbf{u}_i , and $\boldsymbol{\omega}_i$ represent the mass, inertial moment, translational velocity, and angular velocity of particle i , respectively. K is the total number of particles in contact with particle i . The forces acting on particles involve the gravitational force, $m_i \mathbf{g}$, and

inter-particle forces in terms of the normal force, $\mathbf{F}_{n,ij}$, and tangential force, $\mathbf{F}_{t,ij}$, which are determined by the Hertz–Mindlin model.^[17] Torque $\mathbf{T}_{t,ij}$ arises from the tangential forces, while $\mathbf{T}_{r,ij}$ is the rolling friction torque, which is generated by the asymmetric normal contact force.

The parameters used in the DEM simulation are summarized in Table III. The diameters of quaternary granular materials in the simulation are enlarged by a factor of five compared to their actual properties to save computational resources. Therefore, these parameters are first validated by comparing the predicted repose angles with the experimental measurements in Figure 3. The simulation results closely match the experiments, with errors mostly below 5 pct, except for a 7.06 pct error for the alkaline pellets. Overall, the parameters in the simulations effectively capture the granular behaviors of these iron-bearing granular materials.

Besides, a charging matrix labeled as $O_{3,3,4,4,3,2,1,1}^{39,5,38,36,34,32,30,28,30^\circ}$ is used to charge a batch of granular materials. Specifically, the superscripts represent the chute charging angle, which is the angle between the centerlines of the chute and the BF. The subscripts correspond to the number of revolutions performed at each angle. In addition, the rotational speed of the chute is maintained at 8 rpm/min.

IV. RESULTS AND DISCUSSION

A. Instantaneous Basicity Segregation in the BF Charging Process

The charging process can be divided into three primary stages: materials feeding onto the belt, charging into and discharging out of the hopper, and distribution within the throat through the chute in Figure 4(a). As a result, the mass fraction distributions of quaternary iron-bearing materials in the granular mixtures, along with the calculated R_4 distribution, are observed at three locations: the initiation of the feeding belt, the outlet of the parallel hopper, and the end of the chute. These corresponding results are recorded with respect to the dimensionless charging time in Figures 4(b) to (e).

In a batch of granular mixtures, the initial mass fractions of sinters, alkaline pellets, acid pellets, and lump ores are 40, 30, 24, and 6 pct, respectively. The R_4 value for this proportion is calculated to be 1.30. During the first charging stage, from $t = 0$ to 0.3, the quaternary iron-bearing granular materials are sequentially fed onto the belt according to the charging sequences depicted in Figure 4(b). This sequential feeding results in significant fluctuations in the mass fraction and corresponding R_4 along the belt. Specifically, as shown in Figure 4(c), sinters are initially fed onto the belt, followed by alkaline and acid pellets starting at $t = 0.03$. This sequence causes the average R_4 to decrease from 1.75 to approximately 1.27. Subsequently, lump ores are introduced at $t = 0.09$, further reducing the average R_4 to 1.08. At this point, the mass fractions of sinters, alkaline pellets, acid pellets, and lump ores are 29.08, 28.40, 27.68, and 14.84 pct, respectively. Upon

Table III. The Parameters Used in the DEM Simulations

Parameters	Sinters	Alkaline Pellets	Acid Pellets	Lump Ores
Average Diameter, d (m)	0.13	0.08	0.08	0.13
Young's Modulus, E (MPa)	10	10	10	10
Poisson Ratio, ν (-)	0.21	0.25	0.25	0.25
Coefficient of Restitution, e (-)	0.60	0.20	0.20	0.60
Coefficient of Sliding Friction, μ_s (-)	0.43	0.43	0.43	0.43
Coefficient of Rolling Friction, μ_r (-)	0.35	0.50	0.50	0.35

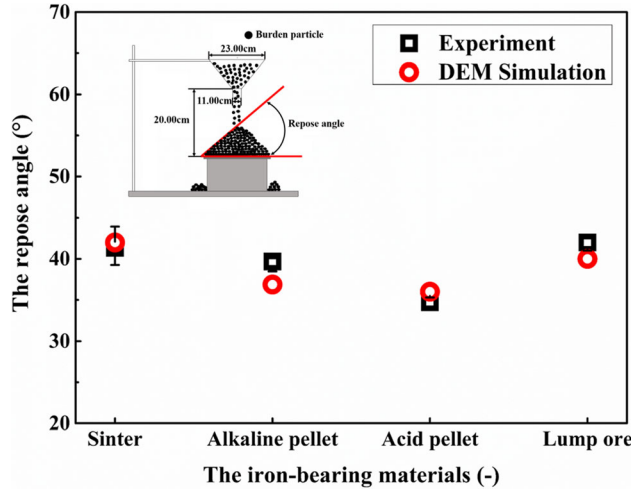


Fig. 3—Comparison of the repose angles between experimental measurements and DEM simulations for quaternary iron-bearing granular materials.

completion of the charging operations for lump ores, acid pellets, and alkaline pellets on the belt at $t = 0.18$, 0.23 , and 0.27 , respectively, the average R_4 steadily increases to 1.27 , 1.58 , and 1.75 in sequence.

Once all granular mixtures have settled within the hopper, the bottom outlet is opened during the second charging stage from $t = 0.48$ to 0.97 (as shown in Figure 4(d)). It is commonly understood that the granular mixtures above the outlet have priority over those close to the walls for being discharged.^[55] Therefore, there are three noteworthy points observed during the discharge process. First, before $t = 0.6$, the mass fractions of sinters and alkaline pellets rapidly decrease at the outlet of the hopper, while the mass fraction of acid pellets continues to increase, eventually reaching a similar level with average values of 35.82 , 32.01 , and 27.83 pct respectively. This results in a continuous decrease in R_4 , followed by slight fluctuations before stabilizing at around 1.3 until $t = 0.8$. Then, from $t = 0.8$ to 0.93 , the mass fraction of sinters abruptly climbs to approximately 62.38 pct and then decreases to around 25.52 pct, while the mass fractions of alkaline and acid pellets continue to decrease to around 16 pct. Since before the end of the belt feeding, all other iron-bearing materials except for the sinter have been fully fed onto the belt based on the charging sequence,

resulting in the sinter becoming the main iron-bearing material on the top of the hopper and leading to R_4 first increasing at 1.52 and then decreasing at around 1.11 . Finally, some other residual iron-bearing materials remained in the hopper due to their location near the walls at the end of charging, causing huge fluctuations in the mass fractions of sinters and alkaline pellets and temporarily increasing R_4 to 1.62 .

Simultaneously, the quaternary iron-bearing materials are distributed in the throat of the BF through a rotating chute. During the third charging stage from $t = 0.5$ to 1.0 , the mass fraction and calculated R_4 below the chute are recorded in Figure 4(e). The mass fraction and R_4 exhibit similar patterns as in the second stage. Therefore, the flow characteristics of iron-bearing granular materials in the BF remain consistent, and these characteristics are determined by the distribution of materials in the hopper.

B. Mapping the Granular Segregation in the Throat

Throughout the three consecutive stages, the quaternary iron-bearing materials are distributed in the BF throat. The cross section of the throat is divided into eight equal sectors in the circumferential direction and six rings with the same area in the radial direction, as illustrated in Figure 5(a). The mass distributions of iron-bearing granular materials and the calculated R_4 in these 48 blocks are quantitatively depicted in Figure 5(b). First, the mass distributions of quaternary iron-bearing granular materials are generally increased in the radial direction. For example, in sector I, the mass of quaternary iron-bearing materials is 491.66 kg in ring I, and it increases to 6388.29 kg in ring V, and then slightly decreases to 5563.44 kg in ring VI. Second, since sinters are the dominant iron-bearing materials in ring I, the calculated R_4 varies from 1.40 to 1.55 . In the remaining regions, the spatial distribution of R_4 mainly falls into two categories. In category C_1 , R_4 ranges from 1.2 to 1.29 across 22 blocks, with an average value of 1.28 . On the other hand, in category C_2 , R_4 varies from 1.3 to 1.39 across 18 blocks, with an average value of 1.32 . In addition, Figure 5(c) illustrates the distribution of R_4 in the throat for these two categories. Category C_2 is primarily concentrated in the center, and at the edges of sector I to sector III of the throats. Consequently, the basicity distribution in the throat is non-uniform.

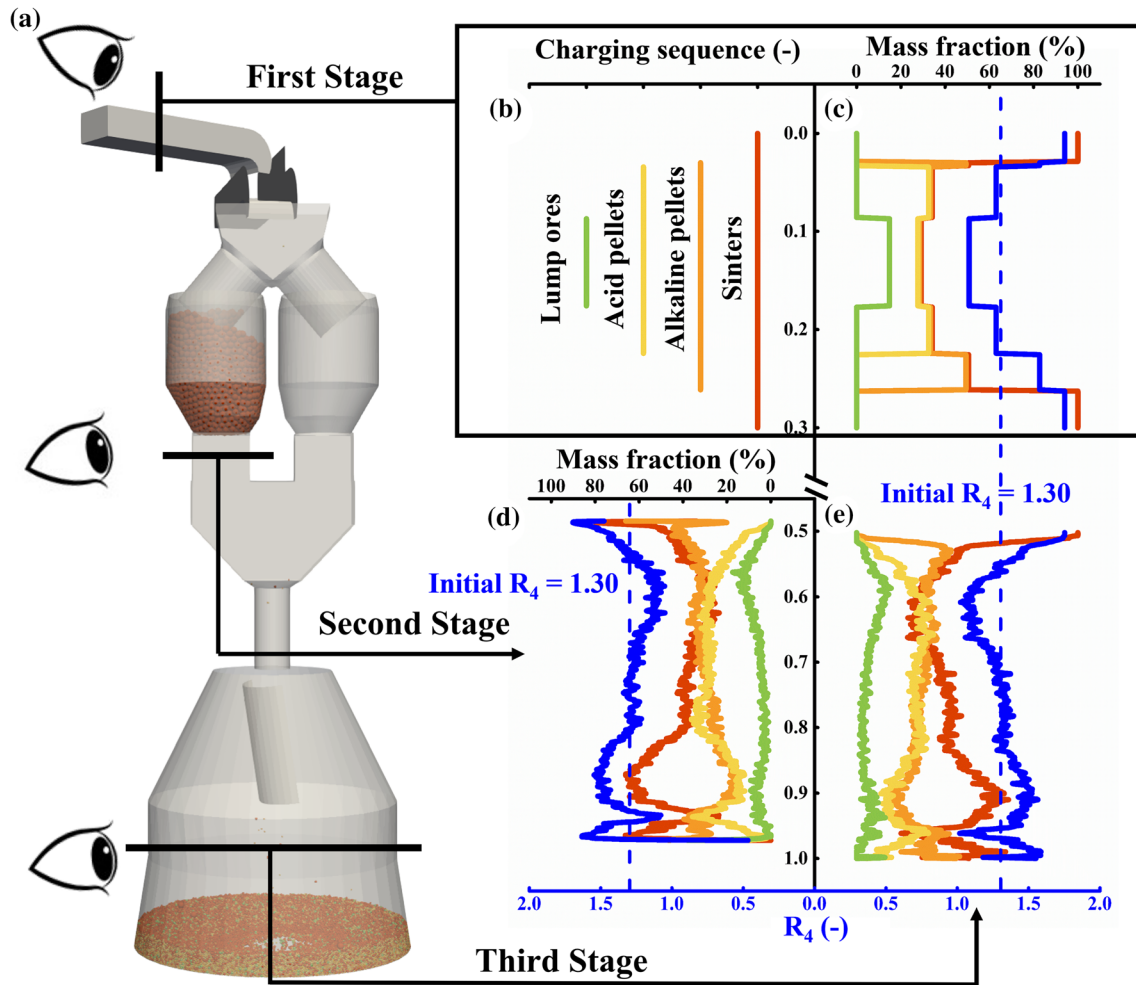


Fig. 4—The mass fraction distributions of quaternary iron-bearing materials, along with the calculated R_4 , with respect to the dimensionless charging time, observed at the initiation of the feeding belt, the outlet of the parallel hopper, and the end of the chute, respectively.

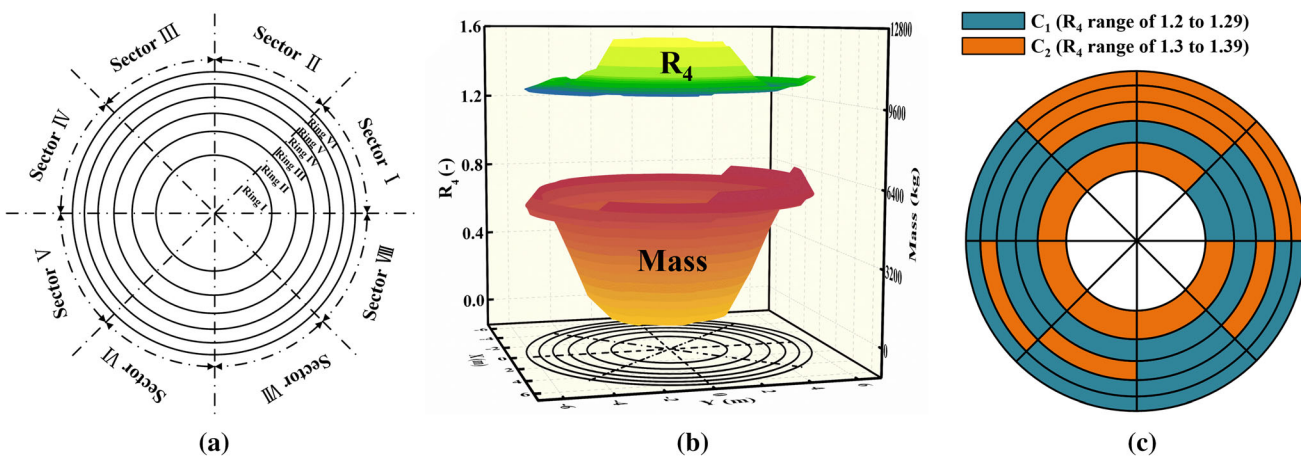


Fig. 5—(a) Schematic diagram of dividing the BF throat into 48 equal blocks, (b) the spatial mass and calculated R_4 distributions of quaternary iron-bearing materials, and (c) The different R_4 categories of quaternary iron-bearing materials at each block of the throat.

Figure 6 presents the mass fractions of quaternary iron-bearing granular materials for categories C_1 and C_2 . In both categories, sinters have the highest mass fraction, while lump ores have the lowest. Notably,

category C_2 exhibits a significantly higher mass fraction of sinters, reaching almost 40 pct or even higher, with an average value that exceeds category C_1 by 3.28 pct. However, the mass fractions of other iron-bearing

granular materials in category C_2 are lower compared to category C_1 . Specifically, for category C_1 , the mass fractions of alkaline pellets and acid pellets range from 27.14 to 33.37 pct and 23.87 to 27.06 pct, respectively. However, lump ores have a mass fraction only ranging from 3.43 to 7.85 pct. Furthermore, the average mass fractions of alkaline pellets, acid pellets, and lump ores for category C_2 are 29.69, 22.84, and 5.79 pct, respectively. These findings indicate that the notable difference between these two categories of iron-bearing materials is determined by sinters.

Hence, in the subsequent section, three typical proportions of iron-bearing materials which include a proportion from each of the two R_4 categories and one initial proportion are selected for the elevated-temperature experiments.

C. Influence of Granular Segregation on Their Performance at Elevated Temperatures

According to the quantitative analysis of the granular segregation in the mapping throat, two typical schemes of quaternary iron-bearing materials with R_4 of 1.28 (denoted as Q-1) for category C_1 and 1.32 (denoted as Q-2) for category C_2 , are established in Table IV, in comparison to the scheme with initial R_4 of 1.3 (denoted by Q-0) and four single-component schemes (denoted as S-0 to S-4).

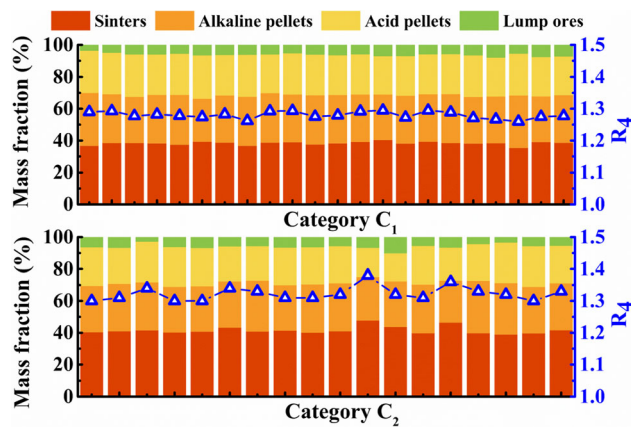


Fig. 6—The mass fraction and calculated R_4 of quaternary iron-bearing materials for categories C_1 and C_2 .

Table IV. The Mass Fractions of Single Iron-Bearing Materials in S-0/1/2/3 Schemes and Quaternary Iron-Bearing Materials in Q-0/1/2 Schemes (Wt Pct)

Scheme	Sinters	Alkaline Pellet	Acid Pellet	Lump Ore	R_4
S-0	100	—	—	—	1.75
S-1	—	100	—	—	1.11
S-2	—	—	100	—	0.36
S-3	—	—	—	100	0.03
Q-0	40	30	24	6	1.30
Q-1	39	30	23	8	1.28
Q-2	42	28	25	5	1.32

The softening and melting behaviors of four single-component schemes and three quaternary-component schemes are measured and compared in Figure 7(a). T_{10} represents the softening beginning temperature at which the samples exhibit a 10 pct reduction in volume, and T_{40} represents the softening ending temperature at which the samples feature a 40 pct reduction in volume. Consequently, the softening range is defined as $\Delta T_1 = T_{40} - T_{10}$. Besides, T_s represents the temperature at which the pressure drop of the packed bed reaches 500 Pa, defining the onset of the melting process. T_d represents the temperature at which the samples start dripping. As a result, the melting range is defined as $\Delta T_2 = T_d - T_s$. Furthermore, ΔP_{max} is defined as the maximum pressure drop of the packed beds above 900 °C, and the results are compared in Figure 7(b).

As depicted in Figure 7, among the single-component schemes, the lump ore (S-3) and acid pellet (S-2), characterized by lower R_4 , exhibit lower T_{10} temperatures at 967.5 °C and 970.9 °C, respectively. As the R_4 increases, the T_{10} temperature correspondingly rises, resulting in comparatively higher T_{10} temperatures for alkaline pellet (S-1) and sinter (S-0), reaching 1051.5 °C and 1036.7 °C, respectively. Furthermore, the sinter and alkaline pellet feature a wider softening range compared to the acid pellet and lump ore. In terms of melting performance, the lump ore and acid pellet exhibit lower T_s temperatures at 1092.9 °C and 1043.6 °C,

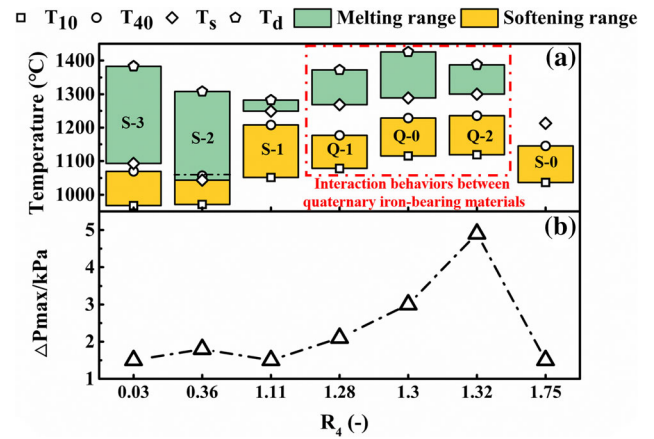


Fig. 7—Comparison of (a) softening and melting behaviors and (b) maximum pressure drop between four single-component schemes (S-0/1/2/3) and three quaternary-component schemes (Q-0/1/2).

respectively, yet possess wider melting ranges of 290.4 °C and 264.5 °C. Conversely, the alkaline pellet and sinter have higher T_s temperatures at 1249.1 °C and 1213 °C, respectively, with the former having a narrower melting range of only 33.2 °C, and no dripping observed for the latter under present experimental conditions. However, all the single-component schemes demonstrate similar ΔP_{\max} values at approximately 1.5 kPa, although the acid pellet has a slightly higher ΔP_{\max} value at around 1.8 kPa.

Moreover, for the quaternary iron-bearing materials schemes, both T_{10} , T_{40} , and T_s temperatures increase with higher R_4 . Despite this, the softening range remains consistent at around 110°C. Conversely, the ΔP_{\max} values increase as R_4 rise, resulting in ΔP_{\max} values of 2.1, 3, and 4.9 kPa for Q-1, Q-0, and Q-2, respectively. Notably, there is a marginal 2 pct increase in lump ore for Q-1 compared to the initial proportion for Q-0, leading to a decrease in the R_4 and a significant reduction in the T_{10} temperature of the quaternary iron-bearing materials. Besides, the proportion of sinter in the quaternary iron-bearing materials has a direct influence on ΔP_{\max} , displaying a linear relationship. For instance, comparing Q-0 with Q-1, which has 1 pct less proportion of sinters in the mixture, there is a corresponding decrease of 0.9 kPa in ΔP_{\max} . Conversely, in the case of Q-2, where the sinter proportion increases by 2 pct compared to Q-0, there is an observed increase of 2.8 kPa in ΔP_{\max} . In summary, except for the sinter, the basicity increases the temperature at which iron-bearing materials start softening. Furthermore, the characteristic temperatures of quaternary-component schemes consistently surpass those of single-component materials, owing to the interaction behaviors between the iron-bearing materials involved. Additionally, Figure 8 illustrates the distribution of softening and dripping temperatures based on transient R_4 in the throat, as well as the distribution simply based on the initial R_4 in a BF. The figure reveals that the actual quaternary iron-bearing materials in the throat exhibit lower softening and dripping temperatures compared to the counterparts associated with the initial iron-bearing materials proportion. Furthermore, in regions characterized by higher R_4 , the softening and dripping temperatures are higher than those characterized by lower R_4 , creating a distinct ‘w’-shaped temperature distribution from the center to the edge in the BF.

V. CONCLUSIONS

This study presents an innovative approach to establishing a quantitative relationship between the physical segregation of quaternary iron-bearing materials during the charging process and the subsequent chemical performance in the BF using DEM simulation and elevated-temperature experiments, with quaternary basicity as a pivotal bridge. The key findings can be summarized as follows.

(1) Our investigation reveals distinct variations in mass fractions and R_4 at different locations in the BF

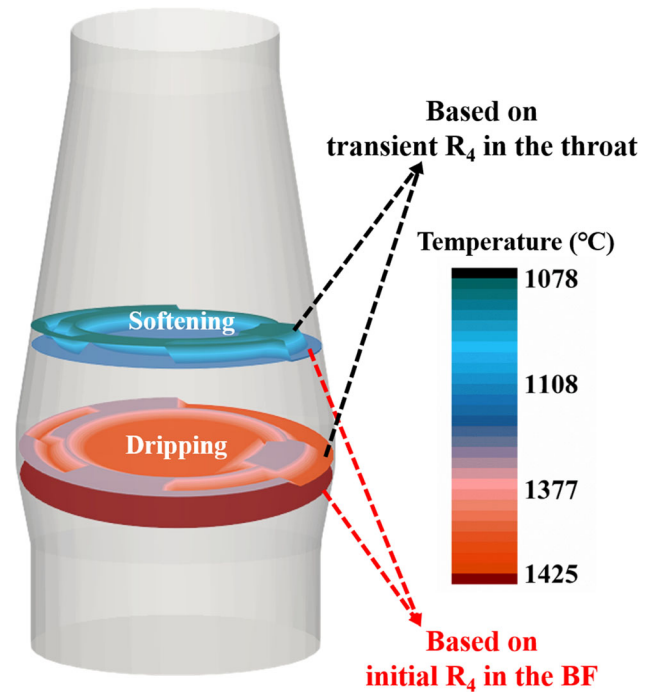


Fig. 8—The comparison of cohesive zone temperature range based on the transient R_4 in the throat and the initial R_4 in the BF.

charging system. The distribution of quaternary iron-bearing granular materials on the feeding belt is significantly influenced by the charging sequence. As a result, the corresponding R_4 varies from 1.75 to 1.08, then to 1.75. This impact propagates throughout the charging process, leading to notable fluctuations in the mass fractions of iron-bearing materials and the determined R_4 at the hopper outlet and the end of the chute. The distribution of granular materials in the hopper is a primary determinant of their flowing characteristics.

- (2) The BF throat is divided into 48 equal-area blocks, revealing a radial increase in the mass distributions of quaternary iron-bearing materials. Notably, the R_4 in these blocks predominantly fall into two categories, C_1 with 22 blocks having an average R_4 of 1.28, and C_2 with 18 blocks having an average R_4 of 1.32. Moreover, the significant difference between these two categories is determined by sinters.
- (3) The softening and melting characteristics of single iron-bearing materials reveal that the materials with lower R_4 exhibit lower softening beginning temperatures, narrower softening ranges, and wider melting temperature ranges compared to materials with higher R_4 . Conversely, quaternary iron-bearing materials demonstrate interaction effects leading to higher T_{10} and T_s temperatures, as well as ΔP_{\max} values, with these values increasing as the R_4 increases. Intriguingly, the softening range temperatures remain consistent across all quaternary iron-bearing material schemes.
- (4) In comparison to previous evaluations of softening and melting behaviors solely based on the initial proportions of iron-bearing materials in the mixture,

this study demonstrates a 'w'-shaped temperature distribution from the center to the edge in the BF by considering the influence of granular segregation during the charging operation.

ACKNOWLEDGMENTS

The authors gratefully acknowledge funding through projects from the Natural Science Foundation of Chongqing, China (Grant Nos. cstc2019jcyj-msxmX0089, cstc2021ycjh-bgzxm0165, cstb2023nscq-msx0514), and Galen scholarship.

CONFLICT OF INTEREST

On behalf of all authors, the corresponding author states that there is no conflict of interest.

REFERENCES

1. D. Proctor, K. Fehling, E. Shay, J. Wittenborn, J. Green, C. Avent, R. Bigham, M. Connolly, B. Lee, T. Shepker, and M. Zak: *Environ. Sci. Technol.*, 2000, vol. 34, pp. 1576–82.
2. Z. Liu, J. Zhang, H. Zuo, and T. Yang: *ISIJ Int.*, 2012, vol. 52, pp. 1713–23.
3. S. Kuang, Z. Li, and A. Yu: *Steel Res. Int.*, 2018, vol. 89, p. 1700071.
4. G. Wang, Z. Liao, Z. Hu, D. Wang, H. Bai, Z. Zou, and J. Xu: *Metall. Mater. Trans. B*, 2022, vol. 53B, pp. 931–37.
5. H. Mio, Y. Narita, S. Matsuzaki, K. Nishioka, and S. Nomura: *Powder Technol.*, 2019, vol. 344, pp. 797–803.
6. Y. Yu and H. Saxén: *Chem. Eng. Sci.*, 2010, vol. 65, pp. 5237–50.
7. C. Ho, S. Wu, H. Zhu, A. Yu, and S. Tsai: *Miner. Eng.*, 2009, vol. 22, pp. 986–94.
8. Y. Yu and H. Saxén: *Steel Res. Int.*, 2013, vol. 10, pp. 1018–33.
9. V. Radhakrishnan and K. Ram: *J. Process. Control.*, 2001, vol. 11, pp. 565–86.
10. L. Shi, G. Zhao, M. Li, and X. Ma: *Appl. Math. Model.*, 2016, vol. 40, pp. 10254–73.
11. H. Zhao, M. Zhu, P. Du, S. Taguchi, and H. Wei: *ISIJ Int.*, 2012, vol. 52, pp. 2177–85.
12. K. Zhou, Z. Jiang, D. Pan, W. Gui, and J. Huang: *Steel Res. Int.*, 2022, vol. 93, p. 2100332.
13. Y. Xu, J. Xu, Z. Liao, Y. Pei, L. Gao, C. Sun, M. Kou, and L. Wen: *Powder Technol.*, 2019, vol. 343, pp. 422–35.
14. H. Mio, M. Kadowaki, S. Matsuzaki, and K. Kunitomo: *Miner. Eng.*, 2012, vol. 33, pp. 27–33.
15. W. Xu, S. Cheng, and C. Li: *Ironmak. Steelmak.*, 2022, vol. 49, pp. 208–16.
16. W. Xu, S. Cheng, Q. Niu, and G. Zhao: *ISIJ Int.*, 2017, vol. 57, pp. 1173–80.
17. Z. Liao, J. Xu, C. Sun, Y. Yang, Y. Pei, M. Kou, Z. Hu, L. Meng, and L. Wen: *Adv. Powder Technol.*, 2020, vol. 31, pp. 670–77.
18. S. Wu, M. Kou, J. Xu, X. Guo, K. Du, W. Shen, and J. Sun: *Chem. Eng. Sci.*, 2013, vol. 99, pp. 314–23.
19. X. Huang, Q. Zheng, A. Yu, and W. Yan: *Powder Technol.*, 2020, vol. 361, pp. 179–89.
20. X. Huang, Q. Zheng, D. Liu, A. Yu, and W. Yan: *Chem. Eng. Sci.*, 2022, vol. 253, p. 117579.
21. J. Chen, H. Zuo, Y. Wang, Q. Xue, and J. Wang: *Metall. Mater. Trans. B*, 2022, vol. 53B, pp. 3793–3804.
22. Z. Hong, H. Zhou, J. Wu, L. Zhan, Y. Fan, Z. Zhang, S. Wu, H. Xu, L. Wang, and M. Kou: *Steel Res. Int.*, 2021, vol. 92, p. 2000262.
23. J. Chen, H. Zuo, H. Zhao, Q. Xue, and J. Wang: *Powder Technol.*, 2022, vol. 409, p. 117845.
24. J. Xu, S. Wu, M. Kou, L. Zhang, and X. Yu: *Appl. Math. Model.*, 2011, vol. 35, pp. 1439–55.
25. M. Kou, J. Xu, S. Wu, H. Zhou, K. Gu, S. Yao, and B. Wen: *Particuology*, 2019, vol. 44, pp. 194–206.
26. B. Dai, J. Yang, F. Liu, X. Gu, and K. Lin: *Powder Technol.*, 2020, vol. 363, pp. 611–20.
27. S. Kumar, S. Khatoon, S. Parashar, P. Dubey, J. Yogi, and A. Anand: *Powder Technol.*, 2023, vol. 427, p. 118682.
28. Z. Deng, Y. Fan, J. Theuerkauf, K. Jacob, P. Umbanhowar, and R. Lueptow: *Powder Technol.*, 2020, vol. 374, pp. 389–98.
29. T. Zhang, J. Gan, A. Yu, D. Pinson, and Z. Zhou: *Powder Technol.*, 2020, vol. 361, pp. 435–45.
30. Y. Yang, C. Sun, Z. Liao, C. Leng, Z. You, and J. Xu: *Powder Technol.*, 2022, vol. 411, p. 117954.
31. C. Li, K. Dong, S. Liu, G. Chandratilleke, Z. Zhou, and Y. Shen: *Powder Technol.*, 2022, vol. 407, p. 117660.
32. W. Xu, S. Cheng, Q. Niu, and G. Zhao: *Ironmak. Steelmak.*, 2017, vol. 46, pp. 105–12.
33. L. Jiao, S. Kuang, A. Yu, Y. Li, X. Mao, and H. Xu: *Metall. Mater. Trans. B*, 2020, vol. 51B, pp. 258–75.
34. X. Dong, A. Yu, S. Chew, and P. Zulli: *Metall. Mater. Trans. B*, 2010, vol. 41B, pp. 330–49.
35. L. Jiao, S. Kuang, Y. Li, X. Mao, H. Xu, and A. Yu: *Metall. Mater. Trans. B*, 2023, vol. 54B, pp. 734–55.
36. X. An, J. Wang, R. Lan, Y. Han, and Q. Xue: *J. Iron. Steel Res. Int.*, 2013, vol. 20, pp. 11–16.
37. P. Nogueira and R. Fruehan: *Metall. Mater. Trans. B*, 2004, vol. 35B, pp. 829–38.
38. P. Nogueira and R. Fruehan: *Metall. Mater. Trans. B*, 2005, vol. 36B, pp. 583–90.
39. P. Nogueira and R. Fruehan: *Metall. Mater. Trans. B*, 2006, vol. 37B, pp. 551–58.
40. B. Lyu, G. Wang, F. Yang, H. Zuo, Q. Xue, and J. Wang: *J. Iron. Steel Res. Int.*, 2023, vol. 30, pp. 2366–77.
41. P. Tan, J. Zhang, J. Huang, Y. Wang, Z. Liu, and F. Han: *Chin. J. Eng.*, 2023, vol. 45, pp. 890–98.
42. T. Li, C. Sun, X. Liu, S. Song, and Q. Wang: *Ironmak. Steelmak.*, 2018, vol. 45, pp. 755–63.
43. F. Silva, L. Lemos, P. DeFreitasNogueira, and M. Bressan: *Metall. Mater. Trans. B*, 2021, vol. 52B, pp. 69–76.
44. C. Loo, L. Matthews, and D. O’dea: *ISIJ Int.*, 2011, vol. 51, pp. 930–38.
45. B. Lyu, G. Wang, L. Zhao, H. Zuo, Q. Xue, and J. Wang: *J. Iron. Steel Res. Int.*, 2023, vol. 30, pp. 227–35.
46. S. Wu, L. Wang, Y. Lu, and K. Gu: *Steel Res. Int.*, 2018, p. 1800041.
47. X. She, J. Wang, J. Liu, X. Zhang, and Q. Xue: *ISIJ Int.*, 2014, vol. 54, pp. 2728–36.
48. S. Wu, H. Han, H. Xu, H. Wang, and X. Liu: *ISIJ Int.*, 2010, vol. 50, pp. 686–94.
49. G. Park, Y. Kang, and J. Park: *ISIJ Int.*, 2011, vol. 51, pp. 1375–82.
50. P. Ma, K. Ma, J. Deng, Q. Wu, and J. Xu: *ISIJ Int.*, 2023, vol. 63, pp. 1957–64.
51. J. Deng, K. Ma, L. Hu, M. Kou, L. Wen, and J. Xu: *Ceram. Int.*, 2020, vol. 46, pp. 11854–60.
52. K. Ma, J. Xu, J. Deng, M. Kou, and L. Wen: *Int. J. Hydrogen Energy*, 2019, vol. 44, pp. 19555–62.
53. K. Ma, J. Xu, J. Deng, D. Wang, Y. Xu, Z. Liao, C. Sun, S. Zhang, and L. Wen: *Metall. Mater. Trans. B*, 2018, vol. 49B, pp. 2308–21.
54. P. Cundall and O.L. Strack: *Géotechnique*, 1980, vol. 30, pp. 331–36.
55. J. Xu, Z. Hu, Y. Xu, D. Wang, L. Wen, and C. Bai: *Powder Technol.*, 2017, vol. 308, pp. 273–89.

Publisher’s Note Springer Nature remains neutral with regard to jurisdictional claims in published maps and institutional affiliations.

Springer Nature or its licensor (e.g. a society or other partner) holds exclusive rights to this article under a publishing agreement with the author(s) or other rightsholder(s); author self-archiving of the accepted manuscript version of this article is solely governed by the terms of such publishing agreement and applicable law.